Z-Contrast Enhancement in Au-Pt Nanocatalysts by Correlative X-ray Absorption Spectroscopy and Electron Microscopy: Implications for Composition Determination

Yang Liu,^{1†} Maichong Xie,^{2†} Nicholas Marcella,¹ Alexandre C. Foucher,³ Eric A. Stach,³

Marc R. Knecht,^{2,4,*} Anatoly I. Frenkel^{1,5*}

- Department of Materials Science and Chemical Engineering, Stony Brook University,
 Stony Brook, New York 11794, USA.
- 2. Department of Chemistry, University of Miami, Coral Gables, Florida 33146, USA
- Department of Materials Science and Engineering, University of Pennsylvania,
 Philadelphia, PA 19104, USA
- 4. Dr. J.T. Macdonald Foundation Biomedical Nanotechnology Institute, University of Miami, Miami, Florida 33136, USA.
- 5. Chemistry Division, Brookhaven National Laboratory, Upton, New York 11973, USA.

† Y.L. and M.X. Equally Contributing Authors

KEYWORDS nanoparticles, peptides, XANES, machine learning, neural network, STEM, EELS

ABSTRACT. The properties of bimetallic nanoparticles vary widely as a function of their composition and size distributions. X-ray absorption fine structure analysis is commonly used to characterize their structure, but its application to elements that are close to each other in periodic table is hampered by poor Z-contrast. We trained an artificial neural network to recognize the partial coordination numbers in Au-Pt nanoparticles synthesized via peptide templating using their X-ray absorption near edge structure spectra. This approach, combined with scanning transmission electron microscopy analysis, revealed unique details of this prototype catalytic system that has different forms of heterogeneities at both the intra- and inter-particle levels. Our method based on the enhancement of Z-contrast of metal species will have implications for compositional studies of bimetallic nanoparticles.

Introduction:

Bimetallic nanoparticles (BNPs) have received tremendous attention due to their use in biomedical, mechanical, pharmaceutical, catalytic, and electrocatalytic many applications. For example, due to their diverse architectural and compositional motifs that can be tuned by design.²⁻⁵ many types of catalytic BNPs have been reported.^{5, 6} In order to rationally design BNPs with desired performance, a descriptor-based approach is being increasingly adopted. With this approach, structural, electronic, and chemical properties are parameterized and their relationship with the BNP performance is determined.^{7,8} A convenient strategy toward understanding structural and compositional properties of the BNPs is to measure their metal-metal coordination numbers (CNs) and use them to estimate the average size and compositional habits (e.g., distinguish between core-shell and random alloys).9, 10 In a typical research program, such information is extracted from an extended X-ray absorption fine structure (EXAFS) experiment, where absorption edges of each A_xB_{1-x} alloy component, A and B, can be independently measured and analyzed, to obtain the partial CNs: N_{A-A} and N_{A-B} (for the A absorption edge), and N_{B-A} and N_{B-B} (for the B absorption edge).

While EXAFS can be readily applied to most BNPs of interest, there is an important class of these structures that contains elements that cannot be easily distinguished. This occurs when the two metals in the BNP are too close in the same row of periodic table (e.g., Pt-Au, Pt-Ir, Cu-Ni, Ag-Pd, etc.). This occurs due to the sensitivity of EXAFS, which cannot discriminate between the backscattering (A or B) species for A-B and A-A pairs (or B-A and B-B pairs) if A and B have similar Z numbers. To further complicate matters,

the absorption edges of the nearby elements in the same row of periodic table often overlap, so that large portions of the EXAFS signals from both edges (e.g., Pt and Au⁹ or Pt and Ir L₃ edges,¹¹ or As K-edge and Au L₃ edge¹²) coexist in the same energy range. One development^{9, 11} is noteworthy, wherein simultaneous EXAFS analysis of overlapping edges was used to disentangle competing contributions from both edges. However, this requires that effective A-M and B-M (where M = A or B) CNs can be obtained, not partial ones, in order to perform detailed compositional analyses.¹³

An attractive alternative approach is to extract CNs from X-ray absorption near edge spectra (XANES), and not from the EXAFS itself. The near edge region of each element's absorption edge has unique sensitivity to the charge state of that element, which may change because of alloying. Thus, if the XANES spectrum measured for an absorption edge of element A can be related to the numbers of A-A and A-B pairs in the nearest neighboring environment, it would result in the same information that cannot be determined by EXAFS. Due to the lack of analytical methods for recovering the partial CNs from XANES, a machine learning (ML) method was recently developed for that purpose. It was shown by us and others that the ML approach can map XANES spectra onto structural descriptors for monometallic, 14, 15 bimetallic, 16, 17 metal oxide systems 18 as well as other application. 19-21 In addition to being a very good alternative to EXAFS, the ML-XANES method stands out as the only tool for analysis of catalysts under in operando conditions, in the liquid phase, or when exposed to high temperature and pressure. This is because EXAFS data are either of poor quality or unavailable. While ML-XANES has been exceedingly helpful in rapid analysis of BNPs under extreme conditions, it has never been used, to the best of our knowledge, for studying BNPs with elements that have poor

Z contrast. Such an approach could prove to be transformational and allow for atomically resolved analyses of an important class of materials, such as nanocatalysts, for which no readily accessible technique other than – as we show directly here – STEM EDS and EELS is available to confirm the atomic arrangement of the metal species.

We have chosen peptide-capped PtAu BNPs for this study, based upon their wide range of potential applications.^{22, 23} To fabricate the BNPs in water, a multistep coreduction process was developed to generate the final materials. They were passivated on the surface using the AuBP2 peptide (WALRRSIRRQSY), previously identified with affinity for Au.²⁴ Each step in the process was monitored to identify the effects of the reaction on the synthesis of the bimetallic structures. Once prepared, the BNPs were examined using the ML-XANES-based approach, which allowed for the resolution of the partial CN values of Pt and Au, which could not be achieved via conventional EXAFS analysis. The results demonstrated that a non-alloyed system was generated with a cluster-in-cluster morphology. In addition, separate monometallic Pt NPs were present in the reaction mixture, which was confirmed with high-resolution STEM-EELS analysis. Such results demonstrate that advanced characterization with atomic resolution was possible for structures not accessible via conventional approaches. Such ML-XANES methods could be adapted for a variety of systems, including in situ analysis, thus advancing knowledge of fundamental structure/property relationships that cannot be presently addressed.

RESULTS AND DISCUSSION:

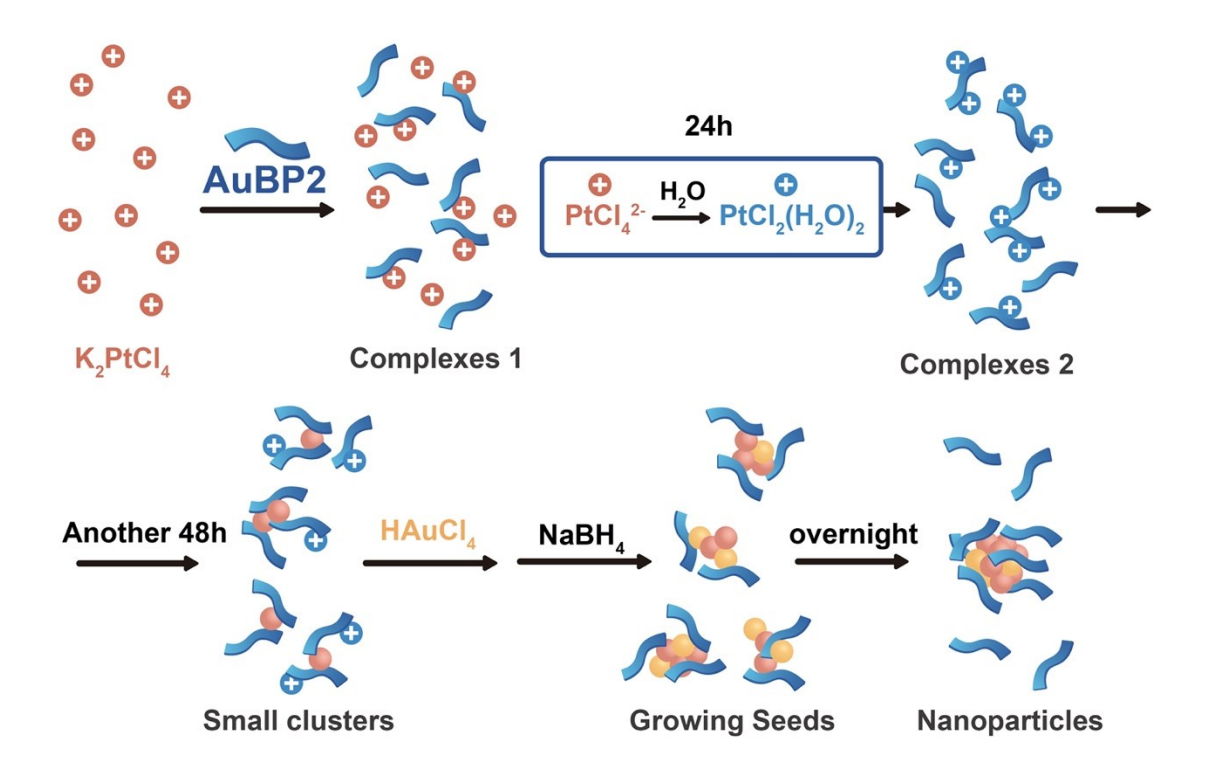
The synthesis procedure developed for AuPt nanoparticles is described in Materials and Methods part of the Supporting Information (SI) and shown in Scheme 1. For this, the

K₂PtCl₄ and AuBP2 peptide were co-mixed in water for 72 h for Pt²⁺ hydrolysis that was required for metal ion binding to the peptide, which was monitored using UV-vis spectroscopy (Figure 1). Specifically shown in Figure 1a, the spectra of the materials prepared at the anticipated Pt:Au ratios are shown immediately after solution production (time = 0 h). For this system, PtCl₄²⁻ ligand-to-metal charge transfer (LMCT) bands were observed at 215 and 230 nm,²⁵ where their intensity was directly proportional to the amount of Pt²⁺ in the mixture. Over time (Figure 1b-d), the intensity of these peaks decreases and the growth of two new peaks at 250 and 305 nm was evident. As anticipated, the intensity of these new bands, which are consistent with coordination of the Pt²⁺ to the peptide amines,^{25, 26} was directly proportional to the amount of Pt in the system. Figure 1e plots the intensity of the 250 nm peak as a function of time and Pt²⁺ concentration, confirming continued growth of the absorbance over the 72 h reaction. Such studies were consistent with the prior results for dendrimer-encapsulated nanoparticles (DENs), where similar reactivity was noted.²⁶

Beyond the LMCT bands associated with the Pt²⁺ ions, two additional points of interest are observed in the UV-vis analysis of Figure 1. For this, however, it is important to note that all of the spectra are background subtracted against the peptide at the reaction concentration. First, two noticeable troughs in the spectra were evident at 225 and 280 nm. For the 225 nm region, the spectra even become negative, suggesting that changes are likely from the peptide itself. Second, over time, a broad increase in absorbance towards lower wavelengths was observed for the sample that is directly proportional to the Pt concentration in the reaction. Taken together, this suggests that the peptide is potentially reducing a fraction of the Pt²⁺ ions to Pt⁰. For the first point, spectral troughs

at 225 and 280 nm, these likely arise from oxidation of the tryptophan residues of the AuBP2 peptide, which drive the Pt²⁺ reduction. Tryptophan is known to reduce metal ions in solution, where it is oxidized to kynurenine.^{27, 28} Tyrosine has also been shown to have the ability to reduce metal ions,^{29, 30} potentially facilitating these observed spectral changes and production of Pt^{0,31} Once the Pt²⁺ is reduced to Pt⁰, nucleation of small Pt⁰ clusters is likely, leading to nanoparticle growth, giving rise to the broad absorbance of the second point.³²

After 72 h of hydrolysis, sufficient Au³⁺ is added to the Pt²⁺/peptide system to achieve the appropriate Pt:Au ratios. The materials were then reduced with excess NaBH₄, generating the stable BNP colloidal suspension. Figure 1f presents the UV-vis spectra of the reduced materials. For all the Pt-containing materials, a broad absorbance band was noted that increased in absorbance towards lower wavelengths, consistent with the formation of BNPs. For the Pt₀Au₁₀₀ sample (*i.e.*, monometallic Au), a plasmon band centered at 530 nm was also observed. Such studies are all fully consistent with nanoparticle formation. It is interesting to point out, however, that the Pt-N LMCT band remains present in the BNP samples. This suggests that the Pt-N interaction remains after reduction, which could arise from the peptide binding to the BNP surface, or potentially from a fraction of the Pt²⁺/peptide complex that remains unreduced.



Scheme 1. Synthesis procedure of the AuBP2 capped Pt/Au nanoparticles.

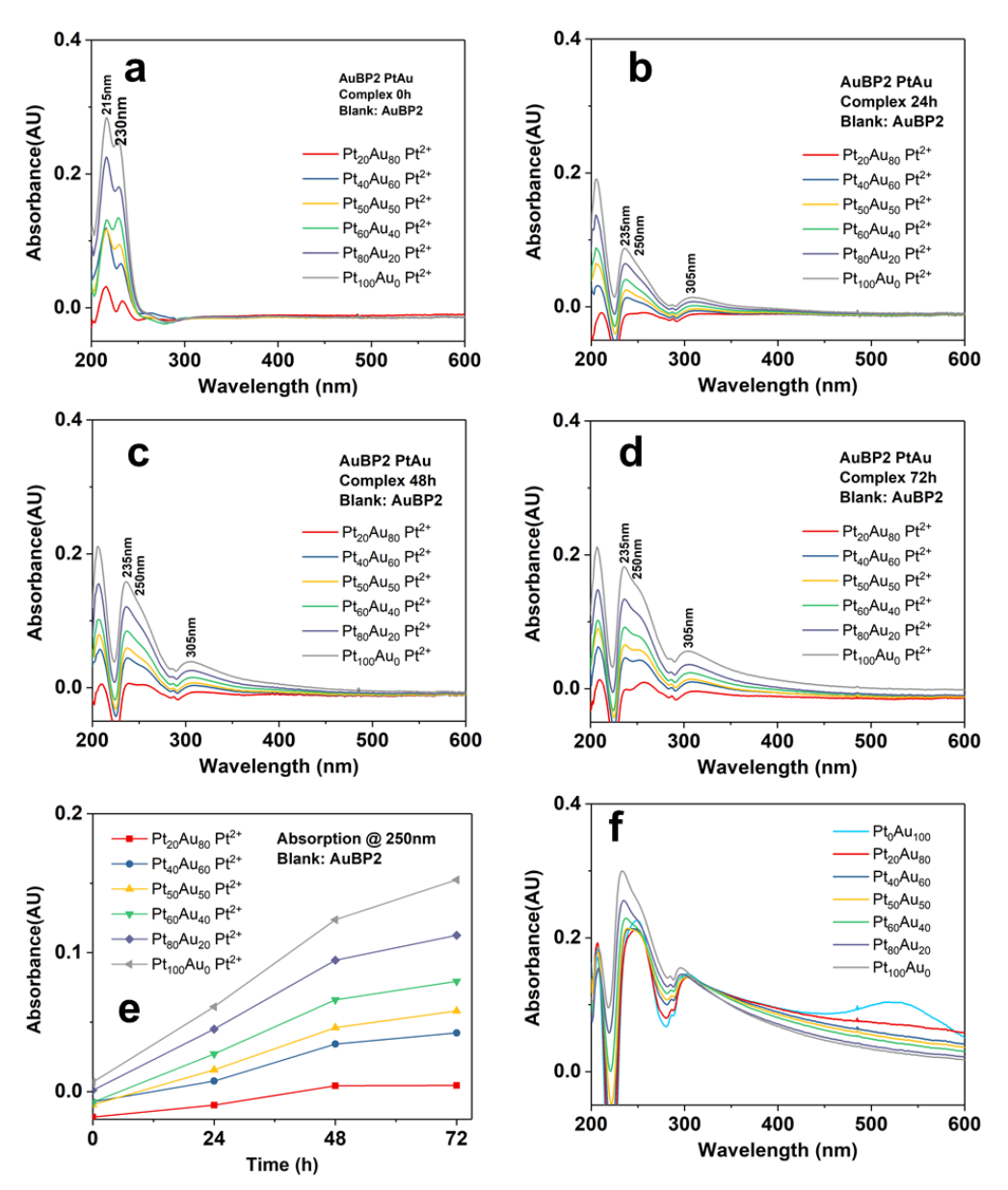


Figure 1. UV-vis analysis of the AuBP2/Pt²⁺ complex at (a) 0h, (b) 24, (c) 48, and (d) 72 h. Part (e) presents the full set of AuBP2-Pt²⁺ complex absorption at 250 nm during the 72 h hydrolysis, while part (f) displays the UV-vis analysis of the reduced BNPs capped with AuBP2.

To confirm that nanoparticle production occurred, HR-TEM analysis of the peptide-capped BNPs was performed (Figures 2 and S1). For all the samples, the nanoparticles were approximately spherical in shape and ranged in size from 2.1 ± 0.4 nm for the $Pt_{80}Au_{20}$ sample to 3.7 ± 0.6 nm for the $Pt_{20}Au_{80}$ system. Analysis of more than 100 individual nanoparticles was performed to identify average particle sizes. Lattice resolved images for each sample, shown in the insets, confirmed that crystalline materials were prepared. No trends between changes in metallic composition and particle size was evident (Figure 2h).

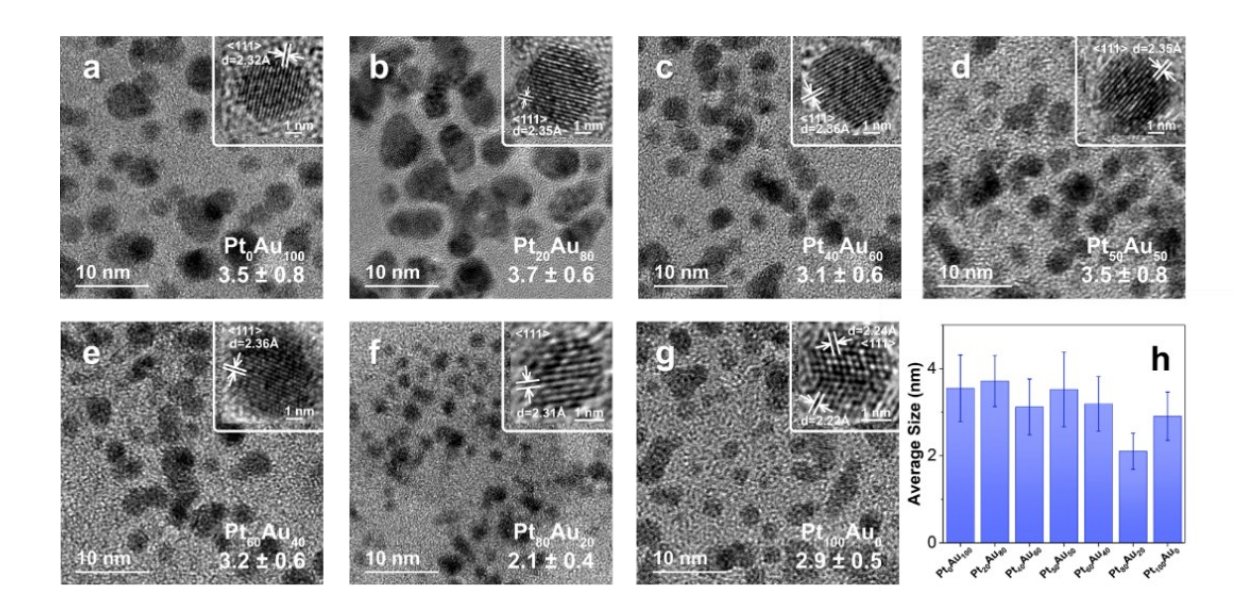


Figure 2. HR-TEM analysis of colloidal PtAu BNPs capped by AuBP2:. (a) Pt₀Au₁₀₀, (b) Pt₂₀Au₈₀, (c) Pt₄₀Au₆₀, (d) Pt₅₀Au₅₀, (e) Pt₆₀Au₄₀, (f) Pt₈₀Au₂₀, and (g) Pt₁₀₀Au₀. Part (h) presents the average BNP sizes of the indicated composition.

XAFS measurements were performed at the ISS (8-ID) beamline National Synchrotron Light Source-II (NSLS-II) at Brookhaven National Laboratory. The solution samples were sealed in Kapton tubes with ~5 mm inner diameter and a wall thickness of

0.2 mm. For each sample 50 scans were collected to improve the data quality. Three samples with different ratios (Pt₈₀Au₂₀, Pt₆₀Au₄₀, Pt₂₀A₈₀) were measured at both Au L₃-edge and Pt L₃-edge. The experimental data are shown in Figure 3. At the Au L₃-edge, there are peak intensity and position changes in the near edge region which are correlated with different Au:Pt ratios; however, at the Pt L₃-edge, the changes are much weaker.

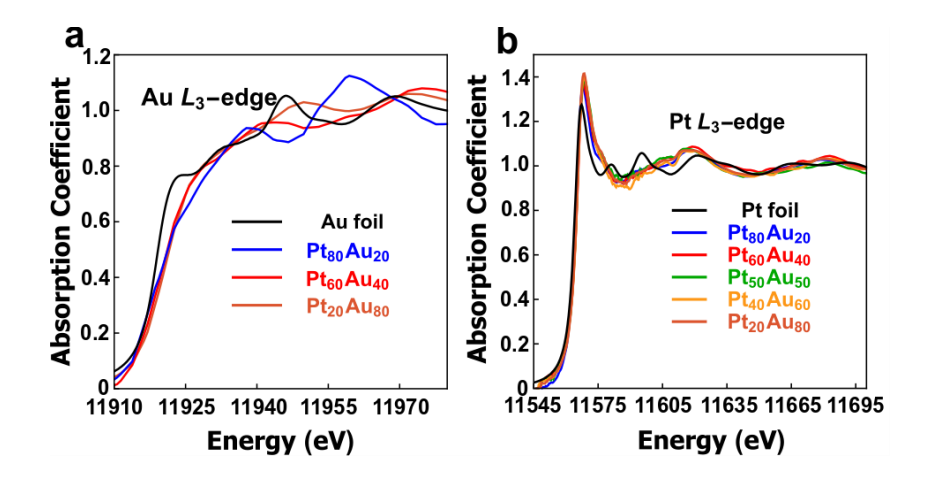


Figure 3. XANES data of Pt_{100-x}Au_x BNPs at (a) Au and (b) Pt L₃ edges.

To quantitively analyze the experimental XANES data and to obtain information about partial CNs of Pt and Au absorbing atoms, the neural network (NN) approach was applied. Detailed information regarding the method is described in Methods part. Similar to our previous work where we correlated the XANES with spectrum with the structural descriptors of Pt and AuPd nanoparticles, 14, 16 the NN was constructed to build a correlation between the XANES spectrum and structural descriptors: Au-Au, Au-Pt, Pt-Au, and Pt-Pt CNs. To train the NN, a large dataset is required to get good performance. Here, we exploited theoretical approaches (FEFF33 and FDMNES34) to construct the training dataset. The standard Au and Pt foils were simulated initially to provide optimized parameters, which are shown in SI, Figure S3. Then the AuPt atomistic models were

constructed based on similar structures and with Au:Pt ratios ranging from 1:9 to 9:1, which covers the composition range of the experimental XANES measurements. To account for the changes of lattice parameters with alloy composition, Vegard's law was used. The effective lattice constants ranged from 3.92 to 4.07 Å (*i.e.*, spanning the range between pure Pt and Au). From this analysis, there were 6578 sites of AuPt atomistic models at the Pt L₃-edge and the 8159 sites of AuPt models at the Au L₃-edge calculated through FEFF and FDMNES. The sites are the different absorbing atoms. In addition, a linear combination approach was employed to enlarge the dataset, as described in our previous study. Using this approach, 100,000 spectra were prepared and randomly shuffled as the total dataset, which was split into an 8:1:1 ratio as training dataset: validation dataset: test dataset. Here the training dataset worked as the major dataset to optimize the parameters in the NN. The validation dataset worked as a benchmark to evaluate the training performance of each training epoch and was used to help optimize the hyperparameters of the NN. The final NN structure is illustrated in Table S1.

To validate the NN and evaluate its performance, a test dataset was exploited (Figure 4). To incorporate the systematic error from the NN models, the error estimation has been given in the SI, section S1. After the NN validation with the test dataset, it was applied to evaluate the experimental XANES spectra. The results for the predicted CNs of Pt-Au, Pt-Pt, Au-Au, and Au-Pt first nearest neighboring pairs are summarized in Table 1. Using these results, the molar ratio of Au:Pt has been calculated as equal to $CN_{Pt-Au}/(CN_{Au-Pt}+CN_{Pt-Au})$. Using the obtained molar fraction of Au atoms, x_{Au} , the Cowley short range order (SRO) parameter was calculated following the equation below:^{13, 35}

$$\alpha = 1 - \frac{cN_{Pt-Au}/(cN_{Pt-Au} + cN_{Pt-Pt})}{x_{Au}}.$$

When the average A-M and B-M CN values are similar, the distribution of elements within the BNPs is considered to be homogeneous; however, if the SRO parameter is positive or negative, this indicates either positive or negative tendency, respectively, to clustering of like atoms. If the SRO parameter is zero, it indicates a random alloy.³⁵ In the present case, however, the results for CN_{Pt-Pt} (Table 1) are intriguing, because they change relatively weakly with composition (also evident in the raw data behavior, Figure 3b) while CN_{Au-Au} values exhibit strong changes. Furthermore, the large Pt-Pt CN values for all compositions (close to the 11-12) appear to be inconsistent with a model of a representative BNP with Pt and Au atoms coexisting in the same particle. This suggests that the distribution of Pt within the sample was bimodal, where some Pt atoms segregate in a separate phase from the PtAu alloyed NPs.

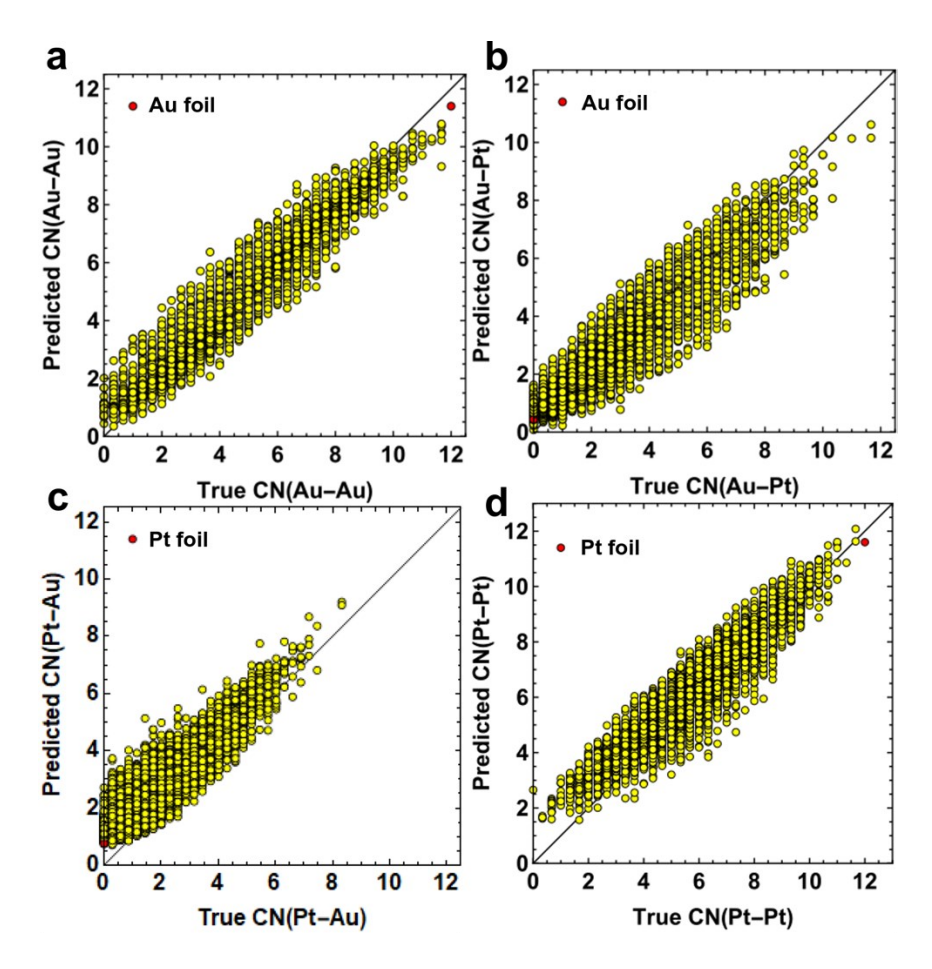


Figure 4. Validation of the neural network using the predicted (a) CN_{Au-Au} , (b) CN_{Au-Pt} , (c) CN_{Pt-Au} , and (d) CN_{Pt-Pt} vs true values.

Table 1. Neural network analysis results of the XANES data at Au L₃-edge and Pt L₃-edge.

Sample	CN _{Pt-Au}	CN _{Pt-Pt}	CN _{Au-Au}	CN _{Au-Pt}	X _{Au}	α	СМм-м
Pt ₂₀ Au ₈₀	1.1±0.8	11.3±0.6	7.8±0.5	0.8±0.6	0.57	0.85	10.2
Pt ₄₀ Au ₆₀	1.2±0.8	11.7±0.6	5.6±0.4	0.6±0.6	0.67	0.86	8.4
Pt ₈₀ Au ₂₀	1.1±0.8	12.0±0.6	0.6±0.5	6.4±0.6	0.15	0.43	12.0

To test this hypothesis and to further validate the ML-XANES analysis results, the High-Angle Annular Dark-Field (HAADF)-STEM and Energy Dispersive Spectroscopy (EDS) analyses were employed to characterize the distribution of Au and Pt atoms in three samples: Pt₈₀Au₂₀, Pt₆₀Au₄₀ and Pt₂₀Au₈₀. The results are summarized in Figures 5 and S5-S8 of the SI. STEM analysis of the samples showed an increased presence of isolated atoms when the Pt concentration was increased. In Figure 5, scattered atoms are visible around Pt₂₀Au₈₀. The EDS spectrum for a region containing only isolated atoms in the Pt₂₀Au₈₀ samples showed that these scattered atoms are mostly Pt, although a minor fraction of Au atoms was also detected (Figure 5). It is important to note that ICP-MS analysis was completed on the sample, where the values obtained generally reflected the ratio of Pt:Au added to the sample.

EDS maps and line scans were performed to visualize the distribution of elements within the tested particles. In all BNP samples studied, a core-shell configuration was observed for most particles, with Pt being segregated on the surface (Figure 5). Additionally, line scans showed the presence of compositional heterogeneity within the particles. In Figure 5a, it is possible to distinguish a Au-rich region on one side of a particle and a Pt-rich region on the other side, which is the evidence of a heterogenous distribution of the alloyed and unalloyed structures.

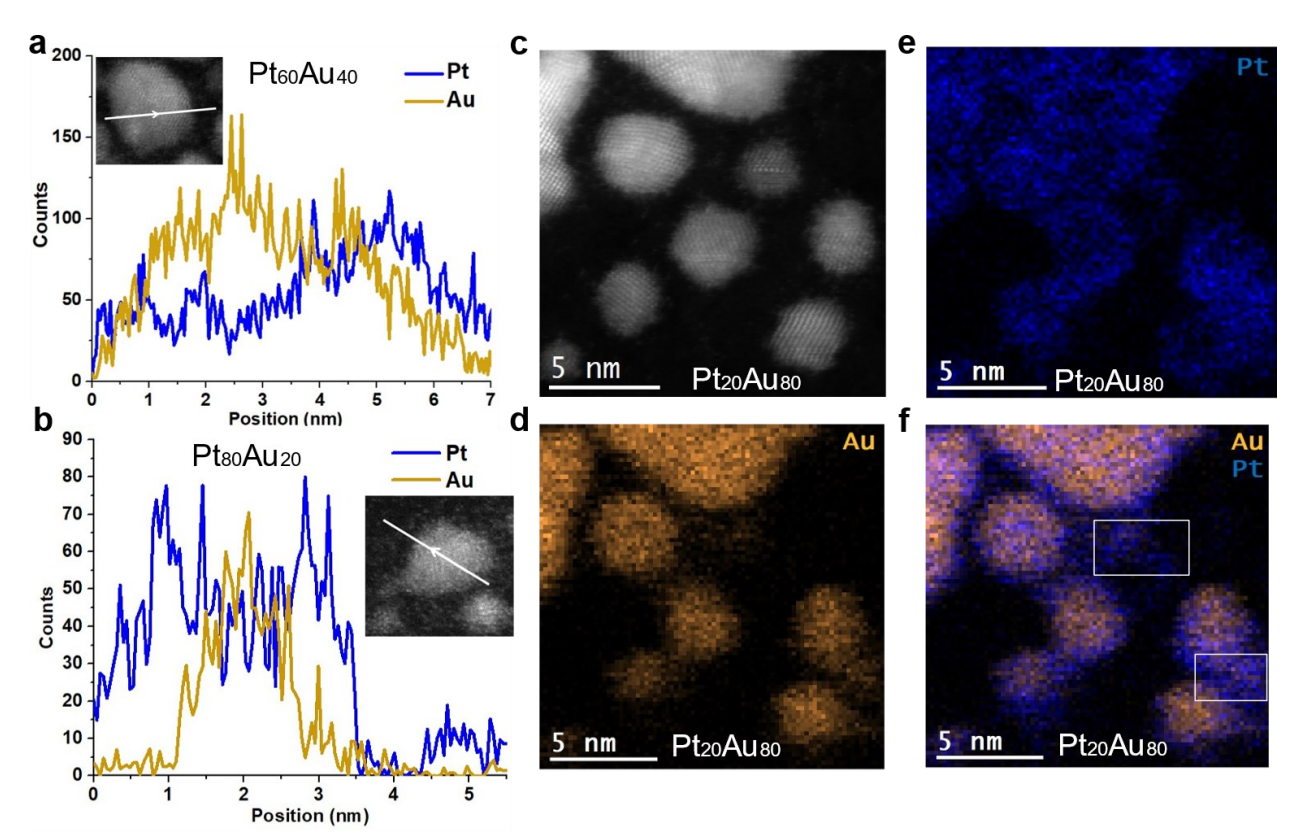


Figure 5. HAADF-STEM imaging and EDS line scan of AuBP2-capped (a) Pt₆₀Au₄₀ and (b) Pt₈₀Au₂₀ BNPs. For part (a), the first half of the BNP is Au-rich while the second half is Pt-rich. The scan is evidence of compositional heterogeneities within the particles. Parts (c-f) presents the HAADF-STEM imaging and EDS mapping of AuBP2-capped Pt₂₀Au₈₀ nanoparticles.

The ability to discern between different models of local structure depends critically on the combination of the ensemble-average information obtained by XAFS and local, statistical information, such as that obtained by STEM-EDS. Without the latter, there are too many possible interpretations of the former when inner particle heterogeneities are present, as we and others have demonstrated earlier.³⁶⁻⁴¹ By combining the information from the EDS mapping and the XANES data, it becomes evident that a bimodal distribution of Pt is present. With more Pt loaded into the sample, a thicker Pt shell structure and isolated Pt particles were observed as shown in Figure 5 and Figures S6-S7 for sample of Pt₂₀Au₈₀, Pt₆₀Au₄₀, and Pt₈₀tAu₂₀. Additional STEM imaging and EDS spectra in Figure S8-S10 also reveal the Pt shell structure with more Au in the core. This effect leads to high CNPt-Pt values and a negligible change in the Pt-Au CNs, as determined by NN-XANES. At the same time, a bimetallic core existed as a heterogeneous Pt-Au alloy with a limited amount of Pt atoms (since even with the larger Pt loading, some of them keep contributing to the shell structure and some - to the separate Pt particles), which explained why the CN_{Au-Au} decreased with the lower Au loading. Thus the correlation between the changes of the CN_{Au-Au} and CN_{Au-Pt} indicate that Au atoms were predominantly distributed in the BNP cores; the relatively unchanged and large CN_{Pt-Pt} values indicate a Pt rich shell and/or coexisting Pt-rich nanoparticles, which are both observed by the EDS mapping. However, due to the limited statistics of EDS mapping, we cannot generalize the observed core-shell motif as the general properties of the entire samples. SI Figures 11-13 show good overall agreement with the trends obtained by the ML-XANES analysis. Indeed, from the Au atoms perspective, they are predominantly co-localized with Pt and thus their coordination numbers are sensitive to the Au:Pt ratios (Table 1). Specifically, CN of Au-Pt increases when the Au:Pt ratio decreases (Table 1). That observation is consistent with the trends shown in Figures S11-S13. Indeed, as the Pt:Au ratio decreases (from 80:20 to 60:40 to 20:80), the relative

amount of Pt in the bimetallic NP region decreases (as evident in SI Figs. 11,12,13, respectively), in agreement with the change of ML-XANES determined CNs of Au-Pt (Table 1).

This bimodal distribution of Pt likely formed due to two reasons: peptide-driven reduction of the Pt²⁺ and the different reduction potentials of the Pt and Au ions employed in the reaction. In the first situation, a fraction of the Pt2+ ions were pre-reduced by the peptide prior to addition of Au³⁺. This likely gives rise to the monometallic Pt particles observed in the samples. In the second situation, Au³⁺ is easier to reduce then Pt²⁺ due to differences in their reduction potentials.⁴² In addition, the Pt²⁺ species were coordinated to the peptide, while the Au³⁺ ions were expected to be free in solution. These differences in reduction potential and local environment could facilitate more rapid reduction of Au³⁺ over Pt²⁺ to give rise to the Au rich core that is then decorated on the surface with the Pt shell upon Pt²⁺ reduction. While electron microscopy analysis provides illustration of such heterogeneous structures at the local scale of individual nanoparticles, the Z-contrast of XANES - which was traditionally limited for Pt-Au (and other alloys with neighboring elements) but is now enhanced by the application of the neural network approach - can also provide information regarding heterogeneity at the scale of the entire ensemble. The combination of NN-XANES and quantitative STEM for this class of BNPs and other heterogeneous nanostructures enables understanding of complex compositional distributions at both the intra- and inter-particle levels.

CONCLUSION:

In summary, combined correlative NN-XANES and HAADF-STEM analysis of peptidecapped BNPs containing neighboring elements such as Pt and Au was used to obtain elusive structural descriptors that helped to elucidate the structural and compositional changes for different ratios of Au:Pt. A bimodal distribution of Pt was discovered with coexistence of AuPt and Pt particles. This method will provide a general solution to a long-standing problem of analysis of structure of other bimetallic nanocatalysts with overlapping absorption energy edges (e.g., Pt-Au, Pt-Ir, Cu-Ni, Ag-Pd, etc.).

MATERIALS AND METHODS:

Synthetic approach for the AuPt nanoparticles with peptide. Production of the peptidecapped PtAu nanoparticles was initially attempted through the direct reduction of HAuCl₄ and K₂PtCl₄ in the presence of the AuBP2 peptide. The Pt:Au ratio was varied to control the final composition of the materials, where the different materials are denoted by Pt_xAu_{100-x}; however, upon reduction with NaBH₄, rapid precipitation of bulk material was observed. Prior studies using dendrimer-encapsulated nanoparticles (DENs) suggested that hydrolysis of the PtCl₄²⁻ ion to PtCl₂(H₂O)₂² was required for complexation to the amines of the polymeric template.² Since similar events were anticipated using the AuBP2 peptide, hydrolysis of the Pt2+ salt was studied for BNP formation. For this, the K₂PtCl₄ was mixed with the AuBP2 peptide in water at selected ratios for 72 h for all syntheses. Using this approach resulted in the production of highly stable peptide-capped BNPs. The AuBP2-capped bimetallic PtAu nanoparticles were synthesized following a modified co-reduction-based method. Seven different nanoparticles were prepared at selected Pt:Au ratios of 0:100, 20:80, 40:60, 50:50, 60:40, 80:20, and 100:0. The description of the synthesis of the Pt₅₀Au₅₀ sample is described; however, identical methods were employed to prepare all of the samples, but with changes in the amount of metal ion salt solutions added to the reaction. Briefly, 1 mL of an aqueous 1 mM AuBP2 solution was diluted with 3.96 mL water. To this mixture, 5 µL of a 100 mM K₂PtCl₄ solution in water was added. The Pt²⁺/AuBP2 solution was then allowed to stir on the benchtop for 3 days at room temperature. Once complete, 5 µL of an aqueous 100 mM HAuCl₄ solution was added to the reaction. After a 15 min incubation time, 30 μL of freshly prepared 100 mM NaBH₄ was added to reduce the metal ions overnight. In all reactions, the ratio of total metal loading:AuBP2:NaBH₄ remained 1:1:3.

UV-vis, TEM and STEM analysis: UV-vis analyses were conducted on an Agilent 8453 spectrophotometer using a 1 cm quartz cuvette. HR-TEM samples were prepared by drop-casting 5 μL of the nanoparticle solution onto a carbon-coated copper TEM grid, which was allowed to dry in desiccator. TEM images were obtained using a Tecnai F30 (FEI) instrument operating at 300 kV. Analysis of >100 individual nanoparticles was used to identify average particle sizes. Scanning transmission electron microscopy (STEM) was performed with a JEOL NEOARM EDS data were collected with detectors provided by JEOL., with a camera length of 4 cm and a condenser lens aperture size of 40 μm. EDS data were collected with detectors provided by JEOL. Elevation angle is 40 °and solid angle is 2.21 steradians. All STEM images were taken right before EDS acquisition. High-angle annular dark field (HAADF) images were collected with a Gatan Inc. detector. The samples prepared for STEM analysis samples were all free-standing particles and directly deposited on the carbon film. A drop of solution was deposited on a carbon coated copper TEM grid from Electron Microscopy Science.

XRD analysis: Powder XRD analyses were conducted using a Bruker D8 ADVANCE powder X-Ray diffractometer with DAVINCI design and a LYNXEYE high-speed 1-D detector. To obtain the necessary nanoparticle powder, all samples were lyophilized to remove the water solvent. XRD result is shown in Figure S2. This analysis compares the XRD patterns of the two monometallic samples (Pt₀Au₁₀₀ and Pt₁₀₀Au₀) to the bimetallic Pt₈₀Au₂₀ material. Scherrer analysis of the XRD data demonstrated that the crystallite

sizes of the samples ranged from 3.0 nm to 2.2 nm (SI Table S2). Therefore, the TEM measured sizes, found to be in agreement with the XRD-determined sizes, are statistically representative of the entire sample. Note that diffractions peaks arising from NaCl were also observed in the sample, which arise from the salts used for the reaction. For the Pt₀Au₁₀₀ peptide-capped nanoparticles, diffractions peaks at 38.4, 44.3, 64.7, 77.8 °20 were evident, arising from the (111), (200), (220), and (311) diffractions peaks of Au, respectively. Conversely, fewer peaks were evident for the Pt monometallic system (Pt₁₀₀Au₀) with the most prominent Pt-based diffraction being observed at 39.9 °20 for the Pt(111) diffraction. For the bimetallic Pt₈₀Au₂₀ peptide-passivated particles, the (111) diffraction peak is at 39.1 °20, which is positioned directly between the (111) diffraction for Au and Pt. This suggests that the BNPs do contain a mixture of the two metals; however, it is not able to distinguish the arrangement of the Pt and Au in the sample. ICP-MS analysis was conducted on an Agilent 7900 ICP-MS.

FEFF and FDMNES simulations. For the neural network assisted XANES analysis, we followed similar approaches as described in the previous work on the monometallic^{14, 15} bimetallic, ^{16, 17} metal oxide systems. ¹⁸ XANES simulations utilized two *ab initio* codes: FEFF³³ and FDMNES. ³⁴ For FEFF simulation, FEFF version 9.6.4 was used for self-consistent calculation within full multiple scattering (FMS) and muffin-tin (MT) approximations. The cluster's radius 5.5 Å was for self-consistent calculation and cluster of radius of 7 Å for FMS calculations. S₀² was optimized as 0.9 Au L₃-edge. Random phase approximation (RPA) was used to model core-hole, as well as complex exchange-correlation Hedin-Lundqvist potential. For FDMENS simulation, we used FDMNES II program, revision 9th. The FMS and MT approximation were applied and real Hedin-

Lundqvist exchange-correlation potential was used for the simulation. The parameters for the simulation were optimized based on the overlap between the experimental and theoretical XANES on the Au and Pt foil, as shown in Figure S3. To show the sensitivity of XANES to the compositional effect, different ratios of Au:Pt of the bimetallic nanoparticles are simulated in the FEFF shown in Figure S4. For the training dataset construction, all the models utilized in our simulation were based on previous work, where the (100) and (111) lattice planes are utilized to cut the bulk and obtain the models with different sizes and shapes. 14 The ratios of Au:Pt were varied from 9:1 to 1:9 and the site of Au and Pt were randomly assigned. The non-equivalent sites in all cluster models were selected for XANES calculation. All theoretical XANES spectra were shifted in energy by ΔE to align the energy scale of theoretical calculations with experimental data. The energy range of Au L3-edge was between 11910 to 11973 eV. The energy range of the Pt L₃edge was between 11562 to 11642 eV. To maximize the variability and increase the size of the dataset, linear combinations of randomly selected site-specific XANES, based on the equations of $\mu(E) = \sum_{j=1}^{n} \mu_j/n$, was utilized to enlarge the XANES-CN datasets where n is optimized to 3 according the NN performance. Then, we randomly selected three XANES-CNs pair from our original site-specific dataset to create 100,000 spectra. For the NN training, the data was split in 8:1:1 as training, validation, and test datasets. The architecture of the NN is described in the Table S1. We used mean squared loss as the metric to evaluate our NN model and the "ADAM" as our optimization algorithm with default parameters ($\beta 1 = 0.9$ and $\beta 2 = 0.99$). To overcome the overfitting, the L2 regularization term has been utilized with 0.001 value. The batch size was optimized to be 800 for our NN models.

ASSOCIATED CONTENT

Supporting Information

AuPt nanoparticle synthesis, UV-vis analysis of the AuPt nanoparticles during the

synthesis, STEM, HAADF-STEM, XRD and EDS mapping analysis of the AuPt

nanoparticles. FEFF and FDMNES simulation of the AuPt nanoparticles. The error

estimation based on the theoretical validation.

AUTHOR INFORMATION

Corresponding Authors

*E-mail: <u>anatoly.frenkel@stonybrook.edu</u>,

*E-mail: knecht@miami.edu;

ORCID:

Yang Liu: 0000-0003-4347-1729

Maichong Xie: 0000-0002-1654-952X

Nicholas Marcella: 0000-0002-2224-532X

Alexandre C. Foucher: 0000-0001-5042-4002

Eric A. Stach: 0000-0002-3366-2153

Marc R. Knecht: 0000-0002-7614-7258

Anatoly I. Frenkel: 0000-0002-5451-1207

22

Notes

The authors declare no competing financial interest.

ACKNOWLEDGMENTS

This contribution has been primarily supported by the National Science Foundation under grants 1903576 (A.I.F.) and 1903649 (M.R.K.). Electron microscopy analysis of A.C.F. and E.A.S. was supported as part of the Integrated Mesoscale Architectures for Sustainable Catalysis (IMASC), an Energy Frontier Research Center funded by the U.S. Department of Energy, Office of Science, Basic Energy Sciences under Award #DE-SC0012573. This research used beamline 8-ID of the National Synchrotron Light Source II, a U.S. Department of Energy (DOE) Office of Science User Facility operated for the DOE Office of Science by Brookhaven National Laboratory under Contract No. DE-SC0012704. This research used resources of the Center for Functional Nanomaterials, which is a U.S. DOE Office of Science Facility, and the Scientific Data and Computing Center, a component of the Computational Science Initiative, at Brookhaven National Laboratory under Contract No. DE-SC0012704. This work was carried out in part at the Singh Center for Nanotechnology at the University of Pennsylvania, which is supported by the NSF National Nanotechnology Coordinated Infrastructure Program under grant NNCI-2025608. Additional support to the Nanoscale Characterization Facility at the Singh Center has been provided by the Laboratory for Research on the Structure of Matter (MRSEC) supported by the National Science Foundation (DMR-1720530). We thank E. Stavitski and D. Leshchev for synchrotron measurements.

References

- 1. Loza, K.; Heggen, M.; Epple, M., Synthesis, Structure, Properties, and Applications of Bimetallic Nanoparticles of Noble Metals. *Advanced Functional Materials* **2020**, *30* (21), 1909260.
- 2. Ferrer, D.; Torres-Castro, A.; Gao, X.; Sepúlveda-Guzmán, S.; Ortiz-Méndez, U.; José-Yacamán, M., Three-Layer Core/Shell Structure in Au-Pd Bimetallic Nanoparticles. *Nano Letters* **2007**, *7* (6), 1701-1705.
- 3. Alayoglu, S.; Zavalij, P.; Eichhorn, B.; Wang, Q.; Frenkel, A. I.; Chupas, P., Structural and Architectural Evaluation of Bimetallic Nanoparticles: A Case Study of Pt-Ru Core-Shell and Alloy Nanoparticles. *ACS Nano* **2009**, *3* (10), 3127-3137.
- 4. Yu, W.; Porosoff, M. D.; Chen, J. G., Review of Pt-Based Bimetallic Catalysis: From Model Surfaces to Supported Catalysts. *Chemical Reviews* **2012**, *112* (11), 5780-5817.
- 5. Zhang, J.; Sasaki, K.; Sutter, E.; Adzic, R. R., Stabilization of Platinum Oxygen-Reduction Electrocatalysts Using Gold Clusters. *Science* **2007**, *315* (5809), 220-222.
- 6. Chen, T.; Rodionov, V. O., Controllable Catalysis with Nanoparticles: Bimetallic Alloy Systems and Surface Adsorbates. *ACS Catalysis* **2016**, *6* (6), 4025-4033.
- 7. Göltl, F.; Müller, P.; Uchupalanun, P.; Sautet, P.; Hermans, I., Developing a Descriptor-Based Approach for CO and NO Adsorption Strength to Transition Metal Sites in Zeolites. *Chemistry of Materials* **2017**, *29* (15), 6434-6444.

- 8. Ghiringhelli, L. M.; Vybiral, J.; Ahmetcik, E.; Ouyang, R.; Levchenko, S. V.; Draxl, C.; Scheffler, M., Learning physical descriptors for materials science by compressed sensing. *New Journal of Physics* **2017**, *19* (2), 023017.
- 9. Frenkel, A. I., Applications of extended X-ray absorption fine-structure spectroscopy to studies of bimetallic nanoparticle catalysts. *Chemical Society Reviews* **2012**, *41* (24), 8163-8178.
- 10. Hwang, B.-J.; Sarma, L. S.; Chen, J.-M.; Chen, C.-H.; Shih, S.-C.; Wang, G.-R.; Liu, D.-G.; Lee, J.-F.; Tang, M.-T., Structural Models and Atomic Distribution of Bimetallic Nanoparticles as Investigated by X-ray Absorption Spectroscopy. *Journal of the American Chemical Society* **2005**, *127* (31), 11140-11145.
- 11. Menard, L. D.; Wang, Q.; Kang, J. H.; Sealey, A. J.; Girolami, G. S.; Teng, X.; Frenkel, A. I.; Nuzzo, R. G., Structural characterization of bimetallic nanomaterials with overlapping x-ray absorption edges. *Physical Review B* **2009**, *80* (6), 064111.
- 12. Liu, J.; Amit, Y.; Li, Y.; Plonka, A. M.; Ghose, S.; Zhang, L.; Stach, E. A.; Banin, U.; Frenkel, A. I., Reversed Nanoscale Kirkendall Effect in Au–InAs Hybrid Nanoparticles. *Chemistry of Materials* **2016**, *28* (21), 8032-8043.
- 13. Frenkel, A. I.; Wang, Q.; Sanchez, S. I.; Small, M. W.; Nuzzo, R. G., Short range order in bimetallic nanoalloys: An extended X-ray absorption fine structure study. *The Journal of Chemical Physics* **2013**, *138* (6), 064202.
- 14. Timoshenko, J.; Lu, D.; Lin, Y.; Frenkel, A. I., Supervised Machine-Learning-Based Determination of Three-Dimensional Structure of Metallic Nanoparticles. *J. Phys. Chem. Lett.* **2017**, *8*, 5091-5098.

- 15. Dias, E. T.; Gill, S. K.; Liu, Y.; Halstenberg, P.; Dai, S.; Huang, J.; Mausz, J.; Gakhar, R.; Phillips, W. C.; Mahurin, S.; Pimblott, S. M.; Wishart, J. F.; Frenkel, A. I., Radiation-Assisted Formation of Metal Nanoparticles in Molten Salts. *J. Phys. Chem. Lett.* **2021**, *12*, 157-164.
- 16. Marcella, N.; Liu, Y.; Timoshenko, J.; Guan, E.; Luneau, M.; Shirman, T.; Plonka, A. M.; van der Hoeven, J. E. S.; Aizenberg, J.; Friend, C. M.; Frenkel, A. I., Neural network assisted analysis of bimetallic nanocatalysts using X-ray absorption near edge structure spectroscopy. *Phys. Chem. Chem. Phys.* **2020**, *22*, 18902-18910.
- 17. Liu, Y.; Halder, A.; Seifert, S.; Marcella, N.; Vajda, S.; Frenkel, A. I., Probing Active Sites in CuxPdy Cluster Catalysts by Machine-Learning-Assisted X-ray Absorption Spectroscopy. *ACS Appl. Mater. Interfaces* **2021,** *13*, 53363-53374.
- 18. Liu, Y.; Marcella, N.; Timoshenko, J.; Halder, A.; Yang, B.; Kolipaka, L.; Pellin, M. J.; Seifert, S.; Vajda, S.; Liu, P.; Frenkel, A. I., Mapping XANES spectra on structural descriptors of copper oxide clusters using supervised machine learning. *J. Chem. Phys.* **2019**, *151*, 164201.
- 19. Carbone, M. R.; Topsakal, M.; Lu, D.; Yoo, S., Machine-Learning X-Ray Absorption Spectra to Quantitative Accuracy. *Physical Review Letters* **2020**, *124* (15), 156401.
- 20. Chen, Z.; Andrejevic, N.; Drucker, N. C.; Nguyen, T.; Xian, R. P.; Smidt, T.; Wang, Y.; Ernstorfer, R.; Tennant, D. A.; Chan, M.; Li, M., Machine learning on neutron and x-ray scattering and spectroscopies. *Chemical Physics Reviews* **2021**, *2* (3), 031301.
- 21. Zheng, C.; Mathew, K.; Chen, C.; Chen, Y.; Tang, H.; Dozier, A.; Kas, J. J.; Vila, F. D.; Rehr, J. J.; Piper, L. F. J.; Persson, K. A.; Ong, S. P., Automated generation

- and ensemble-learned matching of X-ray absorption spectra. *npj Computational Materials* **2018**, *4* (1), 12.
- 22. Zhao, Y.; Ye, C.; Liu, W.; Chen, R.; Jiang, X., Tuning the Composition of AuPt Bimetallic Nanoparticles for Antibacterial Application. *Angewandte Chemie International Edition* **2014**, *53* (31), 8127-8131.
- 23. López-Estrada, O.; Zuniga-Gutierrez, B.; Selenius, E.; Malola, S.; Häkkinen, H., Magnetically induced currents and aromaticity in ligand-stabilized Au and AuPt superatoms. *Nature Communications* **2021**, *12* (1), 2477.
- 24. Hnilova, M.; Oren, E. E.; Seker, U. O. S.; Wilson, B. R.; Collino, S.; Evans, J. S.; Tamerler, C.; Sarikaya, M., Effect of Molecular Conformations on the Adsorption Behavior of Gold-Binding Peptides. *Langmuir* **2008**, *24* (21), 12440-12445.
- 25. Elding, L. I.; Olsson, L. F., Electronic absorption spectra of square-planar chloro-aqua and bromo-aqua complexes of palladium(II) and platinum(II). *The Journal of Physical Chemistry* **1978**, 82 (1), 69-74.
- 26. Knecht, M. R.; Weir, M. G.; Myers, V. S.; Pyrz, W. D.; Ye, H.; Petkov, V.; Buttrey, D. J.; Frenkel, A. I.; Crooks, R. M., Synthesis and Characterization of Pt Dendrimer-Encapsulated Nanoparticles: Effect of the Template on Nanoparticle Formation. *Chemistry of Materials* **2008**, *20* (16), 5218-5228.
- 27. Munro, C. J.; Knecht, M. R., Solution Effects on Peptide-Mediated Reduction and Stabilization of Au Nanoparticles. *Langmuir* **2017**, *33* (48), 13757-13765.
- 28. Si, S.; Mandal, T. K., Tryptophan-Based Peptides to Synthesize Gold and Silver Nanoparticles: A Mechanistic and Kinetic Study. *Chemistry A European Journal* **2007**, *13* (11), 3160-3168.

- 29. Selvakannan, P. R.; Swami, A.; Srisathiyanarayanan, D.; Shirude, P. S.; Pasricha, R.; Mandale, A. B.; Sastry, M., Synthesis of Aqueous Au Core-Ag Shell Nanoparticles Using Tyrosine as a pH-Dependent Reducing Agent and Assembling Phase-Transferred Silver Nanoparticles at the Air-Water Interface. *Langmuir* **2004**, *20* (18), 7825-7836.
- 30. Slocik, J. M.; Naik, R. R.; Stone, M. O.; Wright, D. W., Viral templates for gold nanoparticle synthesis. *Journal of Materials Chemistry* **2005**, *15* (7), 749-753.
- 31. Tan, Y. N.; Lee, J. Y.; Wang, D. I. C., Uncovering the Design Rules for Peptide Synthesis of Metal Nanoparticles. *Journal of the American Chemical Society* **2010**, *132* (16), 5677-5686.
- 32. Creighton, J. A.; Eadon, D. G., Ultraviolet–visible absorption spectra of the colloidal metallic elements. *Journal of the Chemical Society, Faraday Transactions* **1991,** 87 (24), 3881-3891.
- 33. Rehr, J. J.; Kas, J. J.; Vila, F. D.; Prange, M. P.; Jorissen, K., Parameter-free calculations of X-ray spectra with FEFF9. *Physical Chemistry Chemical Physics* **2010**, *12* (21), 5503-5513.
- 34. Bunău, O.; Joly, Y., Self-consistent aspects of x-ray absorption calculations. *Journal of Physics: Condensed Matter* **2009**, *21* (34), 345501.
- 35. Cowley, J. M., Short-Range Order and Long-Range Order Parameters. *Physical Review* **1965**, *138* (5A), A1384-A1389.
- 36. Duan, Z.; Timoshenko, J.; Kunal, P.; House, S. D.; Wan, H.; Jarvis, K.; Bonifacio, C.; Yang, J. C.; Crooks, R. M.; Frenkel, A. I.; Humphrey, S. M.; Henkelman,

- G., Structural characterization of heterogeneous RhAu nanoparticles from a microwave-assisted synthesis. *Nanoscale* **2018**, *10*, 22520-22532.
- 37. Foucher, A. C.; Marcella, N.; Lee, J. D.; Tappero, R.; Murray, C. B.; Frenkel, A. I.; Stach, E. A., Dynamical Change of Valence States and Structure in NiCu3 Nanoparticles during Redox Cycling. *J. Phys. Chem. C* **2022**, *126*, 1991-2002.
- 38. Guan, E.; Foucher, A. C.; Marcella, N.; Shirman, T.; Luneau, M.; Head, A. R.; Verbart, D. M. A.; Aizenberg, J.; Friend, C. M.; Stacchiola, D.; Stach, E. A.; Frenkel, A. I., New Role of Pd Hydride as a Sensor of Surface Pd Distributions in Pd-Au Catalysts. *ChemCatChem* **2019**, *12*, 717-721.
- 39. Li, Y.; Zakharov, D.; Zhao, S.; Tappero, R.; Jung, U.; Elsen, A.; Baumann, P.; Nuzzo, R. G.; Stach, E. A.; Frenkel, A. I., Complex structural dynamics of nanocatalysts revealed in Operando conditions by correlated imaging and spectroscopy probes. *Nat. Commun.* **2015**, *6*, 7583.
- 40. Sun, Y.; Frenkel, A. I.; Isseroff, R.; Shonbrun, C.; Forman, M.; Shin, K.; Koga, T.; White, H.; Zhang, L.; Zhu, Y.; Rafailovich, M. H.; Sokolov, J. C., Characterization of palladium nanoparticles by using X-ray reflectivity, EXAFS, and electron microscopy. *Langmuir* **2006**, *22*, 807-16.
- 41. Zhao, S.; Li, Y.; Liu, D.; Liu, J.; Liu, Y.-M.; Zakharov, D. N.; Wu, Q.; Orlov, A.; Gewirth, A. A.; Stach, E. A.; Nuzzo, R. G.; Frenkel, A. I., Multimodal Study of the Speciations and Activities of Supported Pd Catalysts During the Hydrogenation of Ethylene. *J. Phys. Chem. C* **2017**, *121*, 18962-18972.

42. Choi, H. C.; Shim, M.; Bangsaruntip, S.; Dai, H., Spontaneous Reduction of Metal lons on the Sidewalls of Carbon Nanotubes. *Journal of the American Chemical Society* **2002**, *124* (31), 9058-9059.

For Table of Contents Use Only

